Heliyon 10 (2024) e28710

Contents lists available at ScienceDirect

Heliyon

journal homepage: www.cell.com/heliyon

Research article

Method for predicting the size of $Ni_{1/3}Mn_{1/3}Co_{1/3}(OH)_2$ particles precipitated in a stirred-tank semi-batch crystallizer using CFD and particle agglomeration models

Kazuhiko Tsuchioka [a,*], Kazuhide Hayashi [a], Ryuta Misumi [b,c]

[a] Sumitomo Metal Mining Co., Ltd, Battery Research Laboratories, 17-3, Isoura-cho, Niihama, Ehime, 792-0002, Japan
[b] Division of Materials and Chemical Engineering, Faculty of Engineering, Yokohama National University, 79-5 Tokiwadai, Hodogaya-ku, Yokohama, 240-8501, Japan
[c] Advanced Chemical Energy Research Center, Institute of Advanced Sciences, Yokohama National University, 79-5 Tokiwadai, Hodogaya-ku, Yokohama, Kanagawa, 240-8501, Japan

ARTICLE INFO

Keywords:
Co-precipitation
Particle agglomeration model
Semi-batch reaction crystallization
Turbulent mixing
$Ni_{1/3}Mn_{1/3}Co_{1/3}(OH)_2$

ABSTRACT

$Ni_xMn_yCo_z(OH)_2$ is widely used as a precursor for the cathode active material $LiNi_xMn_yCo_zO_2$ in lithium ion batteries, and the precursor size, which determines the size of the active cathode material, affects the characteristics of lithium-ion batteries. This paper proposes a method for predicting the particle size of $Ni_{1/3}Mn_{1/3}Co_{1/3}(OH)_2$ precipitated by semi-batch reaction crystallization. The distribution of supersaturated components formed in the reactor varies with the reactor scale, feed conditions of the raw material solution, and agitation conditions. Therefore, the method presented in this paper considers the effects of these conditions on particle growth. First, to identify the turbulent dispersion and concentration distribution of the supersaturated components formed in the reaction crystallizer, a computational fluid dynamics (CFD) model was constructed consisting of the governing equations of hydrodynamics and the mass balance equations of the supersaturated components considering the production by neutralization and consumption by precipitation. Next, a model of agglomeration was constructed that focused on the balance of the binding and breaking up energies for the particle pairs. The binding energy was quantified based on the bridging between particle pairs by surface deposition. The breaking up-energy was quantified based on the hydrodynamic forces when the agglomerate passes through the impeller. These models were fitted using experimental results for the final average size of the $Ni_{1/3}Mn_{1/3}Co_{1/3}(OH)_2$ secondary aggregate, which was precipitated in a small-scale stirred-tank type semi-batch reaction crystallizer. The models predicted the experimental results of the final average size in a large-scale crystallizer, with the feeding conditions of the raw material solution and stirring conditions as experimental parameters, within ±20%. The models may be used to analyze semi-batch reaction crystallization systems of $Ni_xMn_yCo_z(OH)_2$ of any composition by adjusting the model parameters according to the procedure developed in this study.

Abbreviations: CFD, Computational fluid dynamics.

* Corresponding author.
E-mail address: kazuhiko.tsuchioka.d5@smm-g.com (K. Tsuchioka).

https://doi.org/10.1016/j.heliyon.2024.e28710
Received 2 March 2024; Received in revised form 22 March 2024; Accepted 22 March 2024
Available online 27 March 2024

Nomenclature

C_ξ	molar concentration of the component ξ mol/m^3
$\overline{C_{\xi,i}}$	averaged molar concentration of the component ξ in region i mol/m^3
$\overline{C_{\xi 0,i}}$	averaged molar concentration of the component ξ in region i under reference conditions mol/m^3
$C_{b,\xi}$	molar concentration of the component ξ in the bulk fluid mol/m^3
$C_{s,\xi}$	molar concentration of the component ξ at the particle surface mol/m^3
D_ξ	molecular diffusion coefficient of the component ξ m^2/s
D_t	turbulent diffusion coefficient m^2/s
$\overline{D_{t,i}}$	averaged turbulent diffusion coefficient in region i m^2/s
$\overline{D_{t0,i}}$	averaged turbulent diffusion coefficient in region i under reference condition m^2/s
d_p	diameter of the primary aggregate m
E_{bi}	binding energy of particle bridging J
E_{bi0}	binding energy of particle bridging under reference condition J
E_{br}	breakup energy of particle bridging J
E_{br0}	breakup energy of particle bridging under reference condition J
F	volumetric flow rate of the raw liquid material m^3/s
h	thickness of the surface deposition layer on particles m
k	turbulent kinetic energy m^2/s^2
L_p	length at which agglomerates are accelerated m
L_{p0}	length at which agglomerates are accelerated under reference conditions m
m_p	mass fraction of the $Ni_{1/3}Mn_{1/3}Co_{1/3}(OH)_2$ precipitated product component −
N_n	number of feed nozzles −
n_p	number density of the $Ni_{1/3}Mn_{1/3}Co_{1/3}(OH)_2$ primary aggregates 1/m^3
P_v	agitation power per unit volume W/m^3
R	radius of the secondary agglomerate or aggregate m
R_0	radius of the secondary agglomerate or aggregate under reference conditions m
r	radius of the primary aggregate m
R_1	neutralization reaction rate mol/m^3 s
R_2	precipitation reaction rate mol/m^3 s
Re	Reynolds number $\left(=\frac{\rho_b u d_p}{\mu}\right)$ −
S	binding area for particle bridging m^2
t	duration time of the reaction operation s
t_{term}	termination time of the reaction operation s
t_i	residence time of the agglomerate in region i s
Sc	Schmidt number $\left(=\frac{\mu}{\rho_b D_\xi}\right)$ −
Sc_t	Turbulent Schmidt number $\left(\frac{\nu_t}{D_t}\right)$ −
Sh	Sherwood number $\left(=\frac{d_p}{\delta}\right)$ −
St	Stokes number $\left(=\frac{\rho_p d_p^2 u}{18\mu L_p}\right)$ -
u	bulk fluid velocity m/s
$\overline{u_i}$	averaged bulk fluid velocity in region i m/s
$\overline{u_{0,i}}$	averaged bulk fluid velocity in region i under reference conditions m/s
V_i	volume of region i m^3
$V_{0,i}$	volume of region i under reference conditions m^3
V_T	liquid volume in crystallizer m^3
Greek	
α_1	model coefficient in Eqs. (4) and (7) −
α_2	model coefficient in Eq. (14) −
α_3	model coefficient in Eq. (17) −
α_4	model coefficient in Eq. (18) −
Γ	surface energy per unit surface area J/m^2
δ	thickness of the boundary layer formed on the particle surface m
ε	turbulent energy dissipation rate m^2/s^3
κ_i	growth rate by surface deposition in region i m/s
μ	viscosity of bulk fluid Pa s

ν_t	turbulent kinematic viscosity m^2/s
ρ_b	density of bulk fluid kg/m^3
ρ_p	apparent density of primary aggregate kg/m^3
τ_d	meso-mixing time scale for turbulent mixing s
Φ_ξ	production and consumption terms of component ξ mol/m^3 s
ω	rotational speed of the impeller 1/s
ω_0	rotational speed of the impeller under reference conditions 1/s

Subscripts

i	index of regions with the same supersaturation −
ξ	index of the chemical component(a: $Ni_{1/3}Mn_{1/3}Co_{1/3}SO_4$, b: NaOH, c: $Ni_{1/3}Mn_{1/3}Co_{1/3}(OH)_2$ dissolved product component, d: Na_2SO_4, e: $Ni_{1/3}Mn_{1/3}Co_{1/3}(OH)_2$ precipitated product component) −

1. Introduction

$Ni_xMn_yCo_z(OH)_2$ is widely used as a precursor for $LiNi_xMn_yCo_zO_2$, the cathode active material in lithium-ion batteries [1–5], and its battery characteristics are substantially affected by the morphology (e.g., internal surface area, porosity, and structure) of the cathode active material [1,3]. Because the morphology is determined by the powder characteristics of the precursor (size distribution, porosity, and apparent density), quantitative understanding of the effects of the scale of the equipment used to synthesize the precursor and the conditions of the reaction operation on the powder characteristics is essential for manufacturing the precursor.

Most of $Ni_xMn_yCo_z(OH)_2$ used as a precursor for cathode active materials is produced by precipitation reaction in a stirred-tank crystallizer for homogeneous mixing. Therefore, numerous experimental studies have been conducted for the precipitation of $Ni_xMn_yCo_z(OH)_2$ in stirred tank-type reaction crystallizers [2,6–9], where $Ni_xMn_yCo_z(OH)_2$ was precipitated under controlled temperature, pH, ammonia concentration in the bulk liquid, and impeller speed conditions to investigate the effect of these conditions on powder characteristics such as precursor size and apparent density. However, it is unclear how the scale of the reaction crystallizer and the turbulent mixing rate affects the particle growth mechanism of $Ni_xMn_yCo_z(OH)_2$.

Several studies have investigated the particle growth during the precipitation of $Ni_xMn_yCo_z(OH)_2$ by simulation model analysis. Barai et al. [10] developed a multiscale computational model to describe the nucleation, primary particle growth, and particle agglomeration behavior in the reaction crystallization of cathode active material precursors. Tsuchioka et al. [11] constructed a simple population balance model that considered the growth of particles via collision and coagulation. The model was used to predict the particle size distribution of $Ni(OH)_2$ precipitated in a stirred-tank continuous reaction crystallizer. However, these models assume homogeneous mixing and do not include the governing equations of hydrodynamics or mass balance equations for the chemical components. Therefore, the variables assigned to the model (surface deposition rate, agitation power, etc.) are averaged over the entire reactor; therefore, the model does not consider the effects of reactor scale-up, distribution of supersaturated components, and flow field on particle growth.

Shiea et al. [12] constructed a CFD model based on governing equations coupled with a population balance model to analyze the particle growth during the reaction crystallization of $Ni_{0.8}Co_{0.1}Mn_{0.1}(OH)_2$ by a multi-inlet vortex mixer. The flow field, mixing state, and supersaturation distribution of the equipment were analyzed by CFD, and the effects of the operating conditions, such as the flow rate and inlet concentration, on the crystallite size were quantified. Although the residence time in this reactor is less than 1 s, some studies that observed the particle growth of $Ni_xMn_yCo_z(OH)_2$ in a stirred-tank reaction crystallizer [2,9] suggested that the particle growth mechanism changes over several tens of minutes after the reaction operation begins. Moreover, because the study was focused on the subject of multi-inlet vortex mixers, the effect of reactor scale-up on particle growth was not discussed.

Zauner and Jones [13,14] analyzed the effects of scale-up, stirring conditions, and feed conditions on the particle growth in a stirred-tank crystallizer using experimental and simulation models for the reaction crystallization of calcium carbonate or calcium oxalate. Focusing on turbulent mixing modes and supersaturation levels, they segregated the crystallizer into two compartments: feed and bulk zones, and they modeled the turbulent mixing and crystallization reaction processes dominant in each zone. In addition, mass and population balances were coupled. The particle sizes predicted by the model agreed well with the experimental results from the scale-up crystallizer (0.3–25 L). The results indicate that clarifying how the supersaturation region and turbulent mixing are distributed in a reaction crystallizer is essential for quantifying the effects of reactor scale-up and operating conditions on the growth of particles produced by reaction crystallization.

The present study discusses a method for modeling the particle growth process of $Ni_{1/3}Mn_{1/3}Co_{1/3}(OH)_2$ precipitated in a stirred-tank semi-batch reaction crystallizer and for predicting the particle size. The details of the model concept are described in Section 2. The particle growth model focuses on agglomeration, which is the main particle growth mechanism that determines the final particle size. In particular, we propose a prediction model that incorporates the effects of the scale-up of the reaction crystallizer (60 and 600 L), distribution of supersaturated components, and turbulent flow field.

2. Outline of the particle growth during the semi-batch $Ni_{1/3}Mn_{1/3}Co_{1/3}(OH)_2$ reaction crystallization and method for predicting the agglomerate size

Fig. 1(a) illustrates the progression of reaction operations during the semi-batch reaction crystallization of $Ni_{1/3}Mn_{1/3}Co_{1/3}(OH)_2$

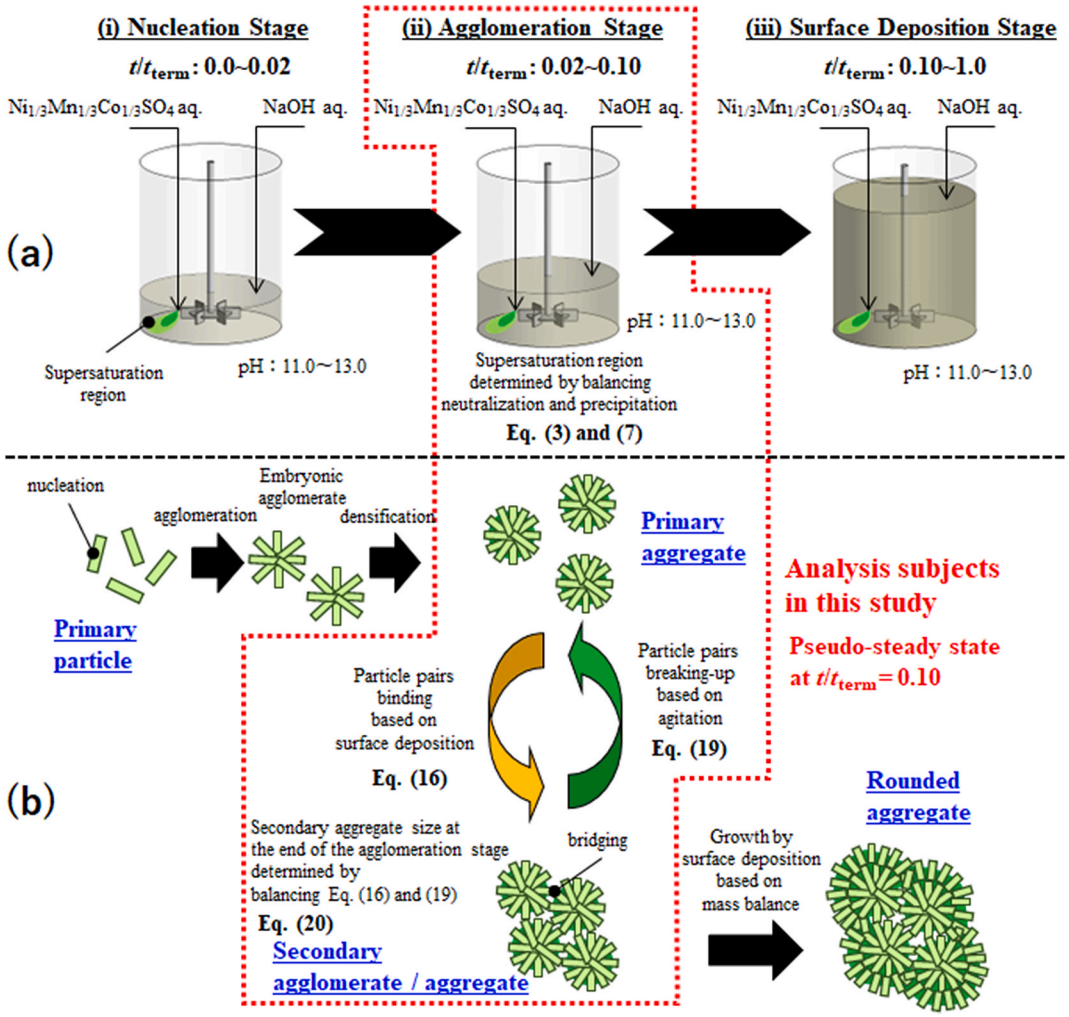

Fig. 1. Outline and analysis of the particle growth during the semi-batch $Ni_{1/3}Mn_{1/3}Co_{1/3}(OH)_2$ precipitation operation. (a) The progression of reaction operation; (b) The schematic of particle growth.

investigated in this study. Generally, an aqueous sulfate solution containing a mixture of transition metal sulfates ($NiSO_4$, $MnSO_4$, and $CoSO_4$) at a composition ratio of 1/3 for each is used as a raw material solution, and an aqueous sodium hydroxide solution is used as a precipitant. An aqueous ammonia solution is also added as a complexing agent. While stirring with the prescribed agitation power, aqueous transition metal sulfate and sodium hydroxide solutions are continuously fed at stoichiometrically equal flow rates to precipitate according to the following reaction equation [6,7,15]:

$$Ni_xMn_yCo_zSO_4 + 2NaOH \rightleftharpoons Ni_xMn_yCo_z(OH)_2 + Na_2SO_4 \quad (1)$$

Simultaneously, sodium hydroxide and ammonia solutions are added continuously to maintain the pH and the ammonia concentration adjusted in the initial bulk solution. As the raw material solution is added, the volume of the bulk solution in the reaction tank gradually increases, and the reaction operation is terminated when the tank capacity is reached.

Yang et al. [9] examined SEM images of $Ni_{1/3}Mn_{1/3}Co_{1/3}(OH)_2$ batch reaction crystallization to detect changes in particle appearance as the reaction progresses. According to these SEM images, at the initial stage of reaction crystallization (t/t_{term}: 0.0–0.1), the $Ni_{1/3}Mn_{1/3}Co_{1/3}(OH)_2$ particles exhibit a bunch of grapes-like structure consisting of small particles. Each particle exhibits a further aggregated structure of plate-like crystals. As the reaction crystallization progresses further (t/t_{term}: 0.1–1.0), the bunch of grapes-like appearance of the particles gradually disappears, and eventually rounded particles are obtained. At this stage, no further agglomeration between particles is observed, and the rounded particles are uniform in size. A similar particle growth process was also observed during the reaction crystallization of $Ni_{0.35}Mn_{0.30}Co_{0.35}(OH)_2$ studied by Koshika et al. [2].

Fig. 1(b) illustrates the particle growth of $Ni_{1/3}Mn_{1/3}Co_{1/3}(OH)_2$. In this study, particles with a bunch of grapes-like structure in the initial stage of reaction crystallization (t/t_{term}: 0.0–0.1) are called "secondary agglomerates" or "secondary aggregates". "Secondary agglomerates" are particles that have just agglomerated and have the potential to separate from each other because the binding

between particles is weak. In contrast, "secondary aggregates" are particles that are no longer likely to separate from each other because the binding between the particles has become sufficiently strong. The grain of bunch of grapes-like particles that compose the secondary agglomerates or aggregates are called "primary aggregates", and the plate-like crystals that compose the primary aggregates are called "primary particles". The particles obtained at the termination of the reaction process are called "rounded aggregates".

Further examination of the SEM images of the appearance of the particles at the initial stage of reaction crystallization (t/t_{term}: 0.0–0.1) obtained by Yang et al. [9] revealed that at the very early stage (t/t_{term}: 0.0–0.02), the size of the individual primary aggregates that compose the secondary agglomerates is not uniform; however, at a later stage (t/t_{term}: 0.02–0.1), the size of individual primary aggregates increases uniformly with the progress of the reaction, and no newly attached small primary aggregates are observed. This feature indicates that in the semi-batch reaction crystallization of $Ni_{1/3}Mn_{1/3}Co_{1/3}(OH)_2$, nucleation occurs only at the very beginning of precipitation (t/t_{term}: 0.0–0.02). The concept of the particle growth of $Ni_{1/3}Mn_{1/3}Co_{1/3}(OH)_2$ proposed by Yang et al. [9] does not consider the mechanism of secondary agglomeration or aggregation; in this study, we restructure the concept of particle growth to include these phenomena.

(i) Nucleation stage (t/t_{term}: 0.0–0.02): Primary particles nucleate and then agglomerate as embryos and grow into primary aggregates. In this study, it is assumed that the $Ni_{1/3}Mn_{1/3}Co_{1/3}(OH)_2$ precipitated during this stage is crystalline and has a uniform compositional distribution of transition metal elements. This assumption is based on the reports that the $Ni_xMn_yCo_z(OH)_2$ obtained by co-precipitation is composed of crystalline phases with a crystal structure similar to that of $Ni(OH)_2$, irrespective of the x, y, and z compositions, and that no clear dissimilar phases are found [2,4,7,9,15].

(ii) Agglomeration stage (t/t_{term}: 0.02–0.1): The primary aggregates further agglomerate to form secondary agglomerates. During this stage, nucleation no longer occurs. We introduced the following hypothesis regarding the mechanism of particle growth by secondary agglomeration. The primary aggregates that collide with each other are first weakly connected through van der Waals forces, and then the connection is strengthened by bridging based on surface deposition. In contrast, hydrodynamic forces based on agitation by the impeller tend to break up the bridging of the particle pairs. The secondary agglomeration repeats until energies based on these action balance. Here, the bridging in secondary agglomerates is further strengthened by surface deposition, and eventually secondary agglomerates become secondary aggregates at the end of the agglomeration stage. An example of an agglomeration model based on the concept of particle bridging and breaking up can be found in the works of Mumtaz et al. [16] and David et al. [17].

(iii) Surface deposition stage (t/t_{term}: 0.1–1.0): The particle growth progresses slowly by only surface deposition on secondary aggregates, eventually forming rounded aggregates. During this stage, the particles should continue to collide with each other, and particle pairs should bridge through surface deposition; however, no further secondary agglomeration is observed in the SEM images of the particle appearance [2,9]. This suggests that as the agglomeration progresses, even if bridging of particle pairs occurs owing to surface deposition, agitation breaks up the bridging, and the success probability of bridging becomes very small; thus, the particles cannot grow in agglomeration. In the semi-batch crystallization of $Ni_{1/3}Mn_{1/3}Co_{1/3}(OH)_2$, once the size and number of secondary aggregates at the end of the agglomeration stage are determined, the final size of rounded aggregates can presumably be estimated from the feed solution mass balance because particles grow only by surface deposition after secondary agglomeration.

Based on the aforementioned, we conducted an analysis to predict the size of secondary aggregates at the end of the agglomeration stage ($t/t_{term} = 0.1$). At this point, the production of primary aggregates has already terminated, and the main particle growth mechanism is secondary agglomeration only. In this study, it was assumed that the final size of secondary agglomerates is determined only by the balance between the binding and breaking energies acting on the agglomerates. Based on this hypothesis, the balance of the number of primary aggregates and the amount of precipitation affects the secondary agglomeration rate but not the final size of secondary agglomerates. In addition, when the size and apparent density of the primary aggregates are constant, it is not necessary to consider the balance of the number of primary aggregates and the amount of precipitation to determine the final size of secondary agglomerates.

Therefore, this study does not consider the balance of the number of particles and the amount of precipitation in the agglomeration stage. The following experiments and modeling were conducted to develop a method for predicting the size of secondary aggregates precipitated by semi-batch reaction crystallization.

Section 3 describes experiments on the reaction crystallization of $Ni_{1/3}Mn_{1/3}Co_{1/3}(OH)_2$. The scale of the reaction crystallizer, feed conditions of the raw material solution, and agitation conditions were used as experimental parameters, and the size of the secondary aggregates of $Ni_{1/3}Mn_{1/3}Co_{1/3}(OH)_2$ at the end of the agglomeration stage was obtained for each of these conditions. Furthermore, the size and shape of the supersaturated region were examined from the traces of precipitated hydroxides adhering to the walls of the reaction tank.

During the agglomeration stage, the distribution of the supersaturated component (concentration and region) and turbulent dispersion (flow velocity and turbulent diffusion) formed in the reaction crystallizer are expected to affect the binding strength of the secondary agglomerates. As described in Section 4, assuming a pseudo steady state in a semi-batch reaction crystallizer at the end of the agglomeration stage ($t/t_{term} = 0.1$), the supersaturated region formed in the crystallizer was quantified using a CFD model based on the balance between the neutralization reaction (Eddy break-up model: reaction model controlled by turbulent mixing) and precipitation reaction (surface deposition model controlled by the mass transfer in the boundary film layer). The balance between the neutralization and precipitation reactions was determined using the experimental results of the precipitation trace described in Section 3.

In Section 5, we discussed a method to determine the diameter of secondary aggregates ($2R$) at the end of the agglomeration stage. As shown in Fig. 1(b), it is assumed that $2R$ is determined proportional to the ratio of the binding energy E_{bi} based on the precipitation reaction to the breakup energy E_{br} based on the agitation action (E_{bi}/E_{br}) in the particle pairs of agglomerates. E_{bi} was evaluated based on the time for secondary agglomerates to pass through the supersaturation region as well as the surface deposition rate in that region. The supersaturation region and turbulent diffusion coefficient substituted in the E_{bi} model were evaluated from the CFD simulation described in Section 4. E_{br} was evaluated based on the centrifugal acceleration acting on the agglomerates as they passed near the impeller.

The reference conditions in the lab-scale experiment are defined, and the diameter of the secondary aggregates at the end of the agglomeration stage under those conditions is $2R_0$. The ratio of $2R$ under any other conditions to $2R_0$ under the reference condition (R/R_0) is assumed to be proportional to the ratio of E_{bi}/E_{br} to E_{bi0}/E_{br0}. The predicted R/R_0 agrees well with the experimental results under eight conditions in which the experimental parameters (scale of the reaction crystallizer, feed conditions of the raw material solution, and agitation conditions) were changed without any additional model parameters.

3. Experimental reaction crystallization of $Ni_{1/3}Mn_{1/3}Co_{1/3}(OH)_2$

3.1. Materials and methods

As illustrated in Fig. 2, the reaction crystallization tank used in the experiment was a stirred tank with a standard flanged dish head with four baffle plates. In this study, a lab-scale tank with 60 L capacity (tank inner diameter: φ420 mm) and scale-up tank with 600 L capacity were used. The impeller, a standard type of the Rushton turbine blades, was placed at the height of the tangent line between the cylindrical part of the tank and the bottom part of the dish. The arrangement and dimensional ratio of the tanks and blades were kept geometrically similar between the lab-scale and scale-up tanks. Eight feed nozzles of mixed transition metal sulfate solution were placed in a concentric circular pattern at equal intervals of 45° above the impeller.

The following four variables were used as experimental parameters in this study: tank diameter, impeller speed, raw material solution feed rate, and number of feed nozzles. The other variables were common to all experimental conditions. During the experimental operation, the initial bulk liquid was first prepared by adjusting the pH to 12.6 with an aqueous NaOH solution and the ammonia concentration to 5 g/L with an aqueous ammonia solution. The volume of the initial bulk liquid was 1/4 of the tank capacity. The pH meter was placed at the positions indicated by a black point in Fig. 2 (near the tank wall, at the midway between the baffle plates, and at the height of the impeller installation). The temperature of the bulk liquid was maintained at 45 °C.

Next, a mixed sulfate solution of $NiSO_4$, $MnSO_4$, and $CoSO_4$ (total concentration 2.3 M, cation ratio Ni:Mn:Co = 1:1:1) was fed at a specified flow rate from a specified number of feed nozzles while stirring at a specified impeller speed under an air atmosphere. Simultaneously, NaOH solution (8.0 M) was dropped onto the position indicated by the purple point in Fig. 2 (in the quadrant opposite the pH meter, near the tank wall, at the midway between the baffle plates, and at the level of the liquid surface) to maintain the pH of the bulk liquid at 12.6. In other words, the feed rate of the NaOH solution was the sum of the reaction equivalent amount shown in Eq. (1) plus a supplemental amount to maintain the pH. Aqueous ammonia solution (13.3 M) was also dropped onto the liquid surface to

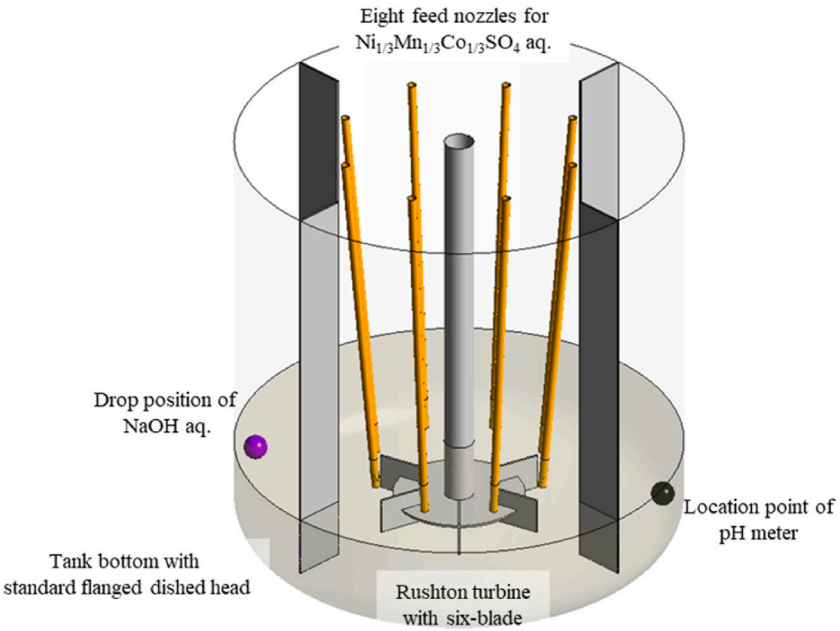

Fig. 2. Schematic of tank layout for $Ni_{1/3}Mn_{1/3}Co_{1/3}(OH)_2$ semi-batch reaction crystallization experiments.

maintain the bulk liquid concentration at 5 g/L.

As described in Section 2, this study set the analysis subjects to the agglomeration stage (t/t_{term}: 0.02–0.1) in the reaction crystallization of $Ni_{1/3}Mn_{1/3}Co_{1/3}(OH)_2$, and particle growth by secondary agglomeration was assumed to be terminate at $t/t_{term} = 0.1$. At this time, the volume of the bulk liquid in the reaction crystallizer increased to 1/3 of the tank capacity. At this point, the bulk liquid was sampled from the reaction crystallizer, and the particle size was measured (MT3300EXII, MicrotracBEL Corp., Japan) to obtain the size of secondary aggregates at the end of the agglomeration stage.

In the experiment, the reference condition (Case A) was liquid volume in crystallizer $V_T = 0.02$ m^3, volumetric flow rate of the raw material solution $F = 2.90 \times 10^{-6}$ m^3/s, number of feed nozzles $N_n = 1$, and rotation speed of the impeller $\omega_0 = 10$ rps. In this study, the types of experimental parameters and their ranges were designed with reference to the case study (precipitation in calcium carbonate and calcium oxalate) by Zauner and Jones [13,14]. Apart from the reference conditions, eight experimental conditions (Cases B–I) were considered, with experimental parameters changed under two conditions (1 and 10) for the ratio of V_T, in the range of 0.67–1.74 for the V_T/F ratio, under three conditions (1, 4 and 8) for N_n, and in the range of 0.4–1.95 for the ratio of the agitation power P_v In these experimental series, geometric similarities were followed with both scales of the reaction crystallizer. Under reference conditions (Case A), the bulk liquid in the reaction crystallizer was removed after the experiment was terminated, and traces of precipitates on the tank walls were photographed.

3.2. Results and discussion

Fig. 3(a) shows the experimental parameters for the precipitation of the $Ni_{1/3}Mn_{1/3}Co_{1/3}(OH)_2$ particles. The experimental parameters included the capacity of the reaction crystallizer V_T, the ratio of the tank capacity to the flow rate of the mixed sulfuric acid solution V_T/F, the number of nozzles feeding the mixed sulfate solution N_n, and the stirring power per unit volume P_v. These parameters were varied as the reference conditions in Case A.

The $Ni_{1/3}Mn_{1/3}Co_{1/3}(OH)_2$ particles obtained in the experiment had a similar morphology as those precipitated by Yang et al. [9]. Specifically, $Ni_{1/3}Mn_{1/3}Co_{1/3}(OH)_2$ particles had a bunch of grapes-like structure consisting of small particles. Each particle exhibited an aggregated structure of plate-like crystals. Fig. 3(b) shows the secondary aggregate size of $Ni_{1/3}Mn_{1/3}Co_{1/3}(OH)_2$ at the end of the agglomeration stage ($t/t_{term} = 0.1$) precipitated under each experimental condition, organized according to the ratio of P_v. The color of the marker classifies the ratio P_v, the shape classifies the ratio V_T/F, and the marker fill type classifies N_n. The size of secondary aggregates in Case A (as the reference condition) $2R_0$ is 4.0 μm. The secondary aggregate size tends to increase as V_T/F decreases, whereas the secondary aggregate size can be reduced by increasing P_v. Furthermore, the secondary aggregate size tends to decrease as N_n increases. In Case C, which has a tank capacity 10 times larger than that of Case B, it was necessary to increase V_T/F and P_v to precipitate the same size secondary aggregate as those in Case B. This effect indicates that scaling up the tank capacity results in an increase in the secondary aggregate size.

Section 5.2.2 discusses the reasons that the secondary aggregates size at the end of the agglomeration stage ($t/t_{term} = 0.1$) changed according to the trend shown in Fig. 3(b) depending on the experimental parameters (flow rate of raw material solution, agitation power, and number of nozzles). In that discussion, we use the simulation result of the distribution of supersaturated components and the turbulent flow field using the CFD model, which is described in detail in Section 4.

(a)

Case	marker	V_T ratio	V_T/F ratio	N_n	P_v ratio
A	○	1	1.00	1	1.00
B	◐	1	1.00	4	1.00
C	◭	10	1.72	4	1.26
D	◭	10	1.72	4	1.70
E	▲	10	1.72	8	1.26
F	◆	10	0.86	4	1.70
G	◆	10	0.86	8	0.40
H	◆	10	0.86	8	1.26
I	◧	10	0.67	4	1.95

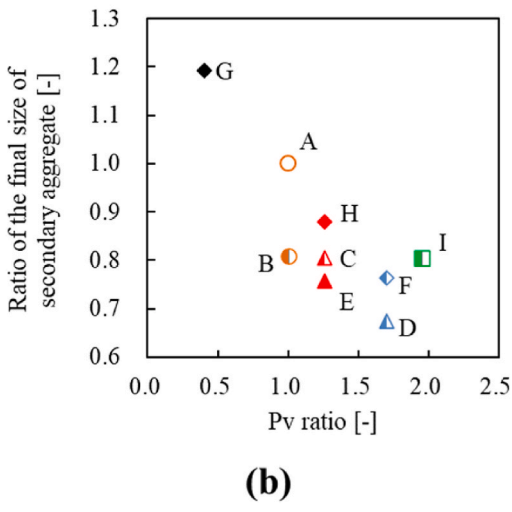

(b)

Fig. 3. Experimental conditions and results for the precipitation of $Ni_{1/3}Mn_{1/3}Co_{1/3}(OH)_2$. (a) Experimental conditions; (b) Experimental results for the final size of secondary aggregates with P_v.

4. Quantification of the concentration and volume of supersaturated region using CFD

4.1. Materials and methods

As described in Section 2, the objective of this study was to predict the size of secondary aggregates at the end of the agglomeration stage ($t/t_{term} = 0.1$). The size of secondary aggregates is determined by the balance between the binding and breaking energies of the particle pairs, which are affected by the distribution of the supersaturation region and turbulent flow field formed in the reactor.

In the reaction crystallization of $Ni_{1/3}Mn_{1/3}Co_{1/3}(OH)_2$ in a stirred-tank reactor, the aqueous solution of $Ni_{1/3}Mn_{1/3}Co_{1/3}SO_4$ fed to the reaction tank reacts immediately with the NaOH solution in the bulk liquid by turbulent mixing to produce the dissolved product component of the transition metal complex hydroxides. The dissolved product component of the hydroxide precipitates quickly as a solid component because of its very low solubility. Therefore, it is estimated that the supersaturated region of $Ni_{1/3}Mn_{1/3}Co_{1/3}(OH)_2$ in the reaction crystallizer is locally distributed near the point where the aqueous solution of $Ni_{1/3}Mn_{1/3}Co_{1/3}SO_4$ is fed, rather than distributed throughout the tank.

However, it is difficult to measure these three-dimensional distributions by experimental methods. Therefore, in this study, CFD based on the governing equations of hydrodynamics and the mass balance of chemical components was used to quantify the distribution of supersaturated regions formed in the reactor.

4.1.1. Geometric model and analysis conditions

As described in Section 3, the semi-batch reaction crystallization of $Ni_{1/3}Mn_{1/3}Co_{1/3}(OH)_2$ requires several hours of reaction operation, and the liquid level in the reactor rises very slowly. In contrast, the reaction rate (neutralization, precipitation, and agglomeration) is very high compared to the speed at which the liquid level rises.

In this study, we quantify the distribution of the pseudo-steady state supersaturated region and turbulent flow field in the reactor (the bulk liquid volume is 1/3 of the tank capacity) at the end of the secondary agglomeration stage ($t/t_{term} = 0.1$). Fig. 4 shows the geometric model used for CFD. The shape of the stirred tank with baffles, the shape and arrangement of the impeller, the arrangement of the feed nozzles of the $Ni_{1/3}Mn_{1/3}Co_{1/3}SO_4$ solution, and the dropping position of the NaOH solution are identical to the those of the reaction tank used in the experiment, as illustrated in Fig. 2. The gas-liquid interface in the liquid-phase section is assumed to be flat, and gas entrainment from the gas-liquid interface owing to stirring is neglected.

In Fig. 4, the part divided into a cylindrical shape by a wire frame surrounding the impeller is the region where the calculation mesh is rotated together with the impeller in the calculation, and it consists of 500,000 hexahedral meshes. The stationary region outside the rotating region consists of hybrid meshes of 1,500,000 tetrahedra and hexahedra. The minimum mesh size was 0.1 mm near the feed nozzle of the raw material solution, and the mesh grew to 3 mm in the bulk area.

The bulk liquid phase as calculation domain was treated as a single-phase fluid consisting of the following six chemical components: The chemical components related to the neutralization reaction were the reaction components (a) $Ni_{1/3}Mn_{1/3}Co_{1/3}SO_4$ and (b)

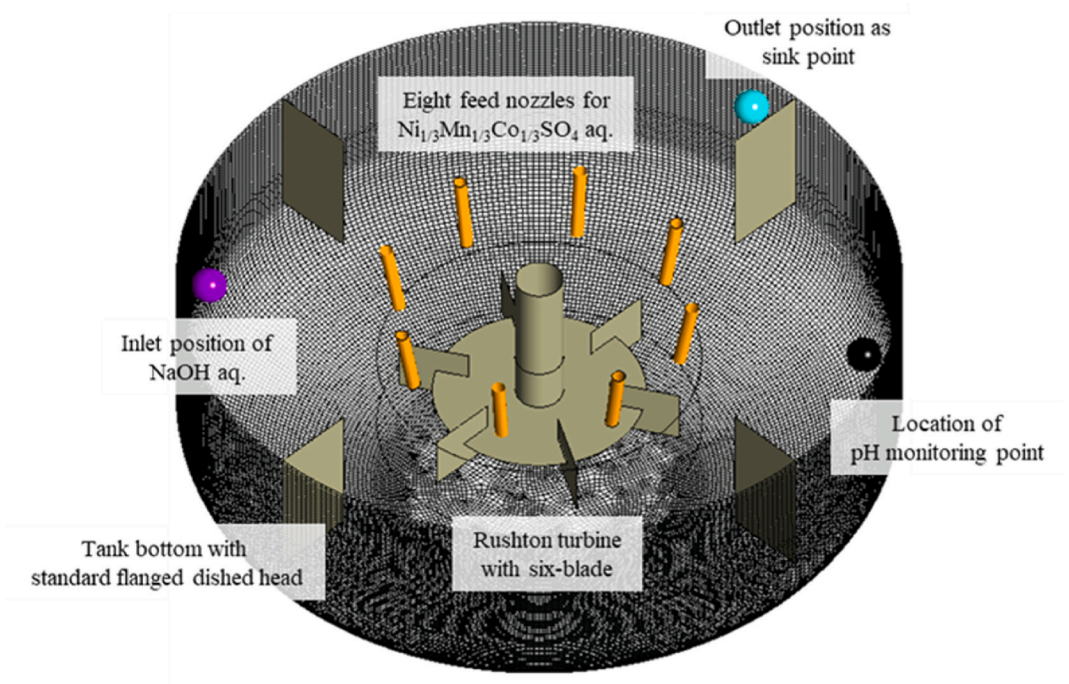

Fig. 4. Geometry model for CFD.

NaOH and the product components $Ni_{1/3}Mn_{1/3}Co_{1/3}(OH)_2$ and (d) Na_2SO_4. For the precipitation reaction, the (e) solid component of $Ni_{1/3}Mn_{1/3}Co_{1/3}(OH)_2$ was defined as the product component, in addition to the (c) dissolved product component of $Ni_{1/3}Mn_{1/3}Co_{1/3}(OH)_2$, which was the reaction component. The remaining chemical component is water, which is not involved in the chemical reactions. Because the *St* number of the particles treated in this study is $\ll 1$, the trajectory of the particles can be regarded as following the fluid flow: Therefore, the $Ni_{1/3}Mn_{1/3}Co_{1/3}(OH)_2$ precipitated product component was assumed to approximate chemical species.

The following Reynolds-averaged mass balance equations were devised for five of these chemical components, excluding water.

$$\frac{\partial\langle C_\xi\rangle}{\partial t}+\langle u_x\rangle\frac{\partial\langle C_\xi\rangle}{\partial x}+\langle u_y\rangle\frac{\partial\langle C_\xi\rangle}{\partial y}+\langle u_z\rangle\frac{\partial\langle C_\xi\rangle}{\partial z}=\left(D_\xi+D_t\right)\left(\frac{\partial^2\langle C_\xi\rangle}{\partial x^2}+\frac{\partial^2\langle C_\xi\rangle}{\partial y^2}+\frac{\partial^2\langle C_\xi\rangle}{\partial z^2}\right)+\Phi_\xi, \tag{2}$$

where $\langle C_\xi\rangle$ (ξ = a,b,c,d,e) is the Reynolds-averaged molar concentration of the chemical components; $\langle u_x\rangle$, $\langle u_y\rangle$, and $\langle u_z\rangle$ are the Reynolds-averaged velocities of the x-, y-, and z-directional components with respect to fluid flow, respectively; D_ξ [m^2/s] is the molecular diffusion coefficient; and D_t [m^2/s] is the turbulent diffusion coefficient. Φ_ξ represents the production and consumption terms of chemical components associated with the neutralization reaction R_1[mol/m^3s] and precipitation reaction R_2[mol/m^3s]. Table 1 summarizes the assignment of index ξ to each chemical component and the notation of the production and consumption terms in the mass balance. The mass balance equation of water was not solved but was considered a constraint, such that the sum of the mass fractions of water and the remaining five components was 1. That is, the model assumes that no hydrate is formed and no water is incorporated when the component e is produced.

The solver used to solve the governing equations of hydrodynamics and the mass balance equations for the chemical components was ANSYS CFX 2022 R1 (ANSYS, Inc.), a commercial fluid analysis software. The SST k-ω model, which is a RANS model, was used to calculate the turbulent flow field [18]. D_t was determined by dividing the turbulent kinematic viscosity ν_t, obtained from a turbulence model of the flow field, by the turbulent Schmidt number Sc_t, which was set to 0.9.

In CFD, we first obtained the steady-state flow field formed by stirring a bulk liquid of 1/3 of the tank capacity ($t/t_{term} = 0.1$) under conditions where there was no inflow of reactant components. The results of this calculation were used as initial conditions for transient state calculations with inflow of reactive components. The concentrations of the $Ni_{1/3}Mn_{1/3}Co_{1/3}(OH)_2$ solid components and Na_2SO_4 components under the initial conditions were set by calculating the chemical reaction equivalent according to Eq. (1) from the total amount of the reaction components fed until $t/t_{term} = 0.1$ in the experiments described in Section 3. The initial concentration of the NaOH component was set to pH = 12.6, as in the experiment.

In the transient-state calculation, the reaction components were assumed to flow from the feeding nozzle of the $Ni_{1/3}Mn_{1/3}Co_{1/3}SO_4$ solution and the drop position of NaOH solution at the same concentration and flow rate as in the experiment shown in Fig. 4. For the feed rate of the NaOH solution, a supplemental amount was added to the chemical reaction equivalent in Eq. (1) to maintain a pH of 12.6 at the monitoring point (black point in Fig. 4). Sink points were placed as outflow boundaries at the blue points shown in Fig. 4. At the sink point, the product components were discharged at a flow rate equivalent to the chemical reaction equivalent of the reactants flowing from the inlet boundary. Similarly, the water component flowing from the inlet boundary was discharged along with the NaOH component. Consequently, the amount of bulk liquid was kept constant as the transient-state calculation proceeded, and the bulk concentrations of the product component and NaOH also remained constant at their initial values. The transient-state calculations progressed toward a pseudo-steady state of the distribution of the supersaturated region and turbulent flow field in the bulk liquid volume of the reactor at $t/t_{term} = 0.1$ (1/3 of the tank capacity).

In transient-state calculation, the calculation progressed with timesteps of 1 ms. The size of the concentration plume of dissolved product components of $Ni_{1/3}Mn_{1/3}Co_{1/3}(OH)_2$ formed in the reactor, i.e., the size of the supersaturated region, was monitored, and when the size of the supersaturated region no longer changed, it was considered that a pseudo-steady state was reached, and the transient-state calculation was stopped. The computer used was an ORION HF210-G2 (Ciara Technologies).

4.1.2. Reaction rate model

4.1.2.1. Production of $Ni_{1/3}Mn_{1/3}Co_{1/3}(OH)_2$ dissolved product components by neutralization. The rate of the neutralization reaction between $Ni_{1/3}Mn_{1/3}Co_{1/3}SO_4$ and NaOH was very high, and the dissolved product component $Ni_{1/3}Mn_{1/3}Co_{1/3}(OH)_2$ formed immediately. Therefore, this study assumed that the overall neutralization reaction was dominated by turbulent mixing processes. In this study, the eddy breakup model of the following equation was adopted as the overall neutralization reaction rate, R_1 [mol/m^3s] [19, 20].

Table 1
Index of chemical components and composition of Φ_ξ terms in Eq. (2).

ξ	Chemical component	Φ_ξ
a	$Ni_{1/3}Mn_{1/3}Co_{1/3}SO_4$	$-R_1$
b	NaOH	$-R_1$
c	$Ni_{1/3}Mn_{1/3}Co_{1/3}(OH)_2$ dissolved product component	R_1–R_2
d	Na_2SO_4	R_1
e	$Ni_{1/3}Mn_{1/3}Co_{1/3}(OH)_2$ precipitated product component	R_2

$$R_1 = \frac{4\varepsilon}{k}\min(C_a, C_b), \tag{3}$$

where k [m^2/s^2] is the kinetic energy of the turbulent flow and ε [m^2/s^3] is the turbulent energy dissipation rate. The parameter k/ε [s] represents the characteristic time corresponding to the lifetime of the turbulence. The reaction rate constant is the reciprocal of this characteristic time. The $Ni_{1/3}Mn_{1/3}Co_{1/3}(OH)_2$ dissolved product component was assumed to be produced in proportion to the concentration of the smaller reactant in the $Ni_{1/3}Mn_{1/3}Co_{1/3}SO_4$ or NaOH components in the calculation cell.

4.1.2.2. Consumption of $Ni_{1/3}Mn_{1/3}Co_{1/3}(OH)_2$ dissolved product components by precipitation. The rate of the precipitation reaction occurring on the surface of the $Ni_{1/3}Mn_{1/3}Co_{1/3}(OH)_2$ particles was assumed to be dominated by the rate at which the $Ni_{1/3}Mn_{1/3}Co_{1/3}(OH)_2$ dissolved product component was transported to the particle surface. When the $Ni_{1/3}Mn_{1/3}Co_{1/3}(OH)_2$ dissolved product component is transported to the particle surface via molecular diffusion, the precipitation reaction rate R_2 [mol/m^3s] in the calculation cell is expressed by the following equation:

$$R_2 = \alpha_1 n_p \pi d_p^2 D_c \frac{(C_{b,c} - C_{s,c})}{\delta}, \tag{4}$$

where n_p [$1/m^3$] is the number density of the $Ni_{1/3}Mn_{1/3}Co_{1/3}(OH)_2$ primary aggregates, and d_p [m] is the diameter of the primary aggregates. D_c [m^2/s] is the molecular diffusion coefficient of the $Ni_{1/3}Mn_{1/3}Co_{1/3}(OH)_2$ dissolved product component, $C_{b,c}$ [mol/m^3] is the bulk concentration of the dissolved product component, $C_{s,c}$ [mol/m^3] is the concentration of the dissolved product component at the aggregate surface, δ [m] is the thickness of the boundary layer formed on the aggregate surface. α_1[-] is the adjustment parameter in the reaction model.

In this study, the *Sh* number was calculated using the Ranz-Marshall formula $Sh = 2.0 + 0.6Re^{1/2}Sc^{1/3}$, where the *Sh* number is the ratio of the thickness of the boundary layer δ to the representative length d_p [21].

By examining the SEM images of the appearance of the $Ni_{1/3}Mn_{1/3}Co_{1/3}(OH)_2$ particles at the end of the agglomeration stage ($t/t_{term} = 0.1$) obtained by Yang et al. [9], the size of the primary aggregates comprising the secondary aggregates were approximately 1 μm. And the apparent density of primary aggregates was estimated to be approximately 2.0 g/mL. This value was estimated from the tapped density of 1.1–1.8 of $Ni_{1/3}Mn_{1/3}Co_{1/3}(OH)_2$ particles precipitated at relatively high pH conditions reported by Lee et al. [6], and the random packing density of the spheres of 0.64 reported by Bernal and Mason [22]. Because pH and temperature are controlled at the same value under all operation conditions, the size and apparent density of primary aggregate is assumed to be constant. Based on these values, the *Re* number of the primary aggregate would be less than 0.001. Therefore, the *Sh* number can be regarded as 2.0, and the thickness of the boundary layer δ can be expressed using Eq. (5).

$$\delta = d_p/2. \tag{5}$$

n_p is expressed by the following equation based on the density of the slurry containing aggregates ρ_b [kg/m^3-solution], the mass fraction of the $Ni_{1/3}Mn_{1/3}Co_{1/3}(OH)_2$ precipitated product component m_p[-], and the apparent density of aggregates ρ_p [kg/m^3-solid]:

$$n_p = \frac{m_p \rho_b}{\rho_p \frac{\pi}{6} d_p^3}. \tag{6}$$

Substituting Eqs. (5) and (6) into Eq. (4), the surface deposition rate is expressed by the following equation.

$$R_2 = 12\alpha_1 \frac{D_c}{\rho_p d_p^2} m_p \rho_b (C_{b,c} - C_{s,c}). \tag{7}$$

In this precipitation reaction model, particles circulating in the reaction crystallizer are assumed to be individual primary aggregates that constitute secondary agglomerate. By confirming the appearance of the particles obtained during the $Ni_{1/3}Mn_{1/3}Co_{1/3}(OH)_2$ reaction crystallization experiment conducted by Yang et al. [9] and the $Ni_{0.35}Mn_{0.30}Co_{0.35}(OH)_2$ reaction crystallization experiment conducted by Koshika et al. [2], it was found that at the end of the agglomeration stage, the size of the primary aggregates comprising secondary aggregates were approximately 1.0 μm. Based on these previous studies, d_p was set to 1.0 μm in this study. In this study, D_c was set as 10^{-9} m^2/s. The apparent density ρ_p of the primary aggregates was set to 2.0 g/mL. Nickel, cobalt, and manganese hydroxides are insoluble in aqueous alkaline solutions and have extremely low solubilities. However, the CFD results shown in the next section 4.2. reveal that the bulk concentration of the $Ni_{1/3}Mn_{1/3}Co_{1/3}(OH)_2$ dissolved product component in the supersaturated region is sufficiently high compared with its solubility. Therefore, in this study, the driving force for the molecular diffusion ($C_{b,c}$-$C_{s,c}$) was approximated as C_c. ρ_b, m_p, and C_c in Eq. (7) were variables calculated using CFD.

4.1.2.3. Comparison of the neutralization and precipitation reaction rates. The size of the plume of the $Ni_{1/3}Mn_{1/3}Co_{1/3}(OH)_2$ dissolved product component, which is a supersaturated component, was determined by the balance between the neutralization reaction rate (Eq. (3)) and the precipitation reaction rate (Eq. (7)) described in the previous sections. If the neutralization reaction rate increases relative to the precipitation reaction rate, the plume will be larger, and vice versa. To accurately calculate the concentration distribution of the $Ni_{1/3}Mn_{1/3}Co_{1/3}(OH)_2$ dissolved product component using CFD model, it is necessary to appropriately adjust the magnitude of the relationship between the neutralization and precipitation reaction rates.

Determining the model coefficients for neutralization and precipitation reaction rates requires experimental measurements to

identify these coefficients; the experimental measurements are often difficult to perform. For example, a model coefficient of 4 in the eddy breakup model proposed by Magnussen and Hjertager [19] was adopted to express the neutralization rate model (Eq. (3)).

However, it is necessary to verify whether a model coefficient of 4 is appropriate, even when this model is applied to neutralization reactions. In another example, in the expression of the precipitation reaction model (Eq. (7)), this study estimates the boundary layer thickness δ based on the Ranz-Marshall formula. However, the $Ni_{1/3}Mn_{1/3}Co_{1/3}(OH)_2$ particles should be smaller than the minimum size of the eddies constituting the turbulent flow field and this effect should be considered. Furthermore, the surface deposition model (Eq. (7)) assumes that the primary aggregates are spheres and considers the surface of the sphere as the deposition area. However, actual primary aggregates have complex surfaces with dense networks of plate-like crystals [9]. Therefore, the deposition area must be larger than the surface area of the spheres. Moreover, the consolidation and surface smoothing of the deposition layer resulting from the re-crystallization process, which occurs according to the Kelvin equation due to the difference in the radius of curvature of the irregularities on the particle surface [9], is also considered to affect the precipitation reaction rate.

In this study, the assumptions mentioned above were included in the process of determining the model coefficients. The discrepancy from the true phenomenon caused by these assumptions is summarized in the model coefficient α_1 of Eq. (7).

4.2. Results and discussion

The model parameter α_1 in Eq. (7) was determined by comparing the CFD-calculated contact area of the plume of the $Ni_{1/3}Mn_{1/3}Co_{1/3}(OH)_2$ dissolved product component on the tank walls with the shape of the $Ni_{1/3}Mn_{1/3}Co_{1/3}(OH)_2$ precipitation traces observed in the experiments described in Section 3. Fig. 5(a) shows the $Ni_{1/3}Mn_{1/3}Co_{1/3}(OH)_2$ precipitation traces observed at the bottom of the reaction tank when the tank was emptied after reaction crystallization experiments under reference conditions (Case A). When the reaction operation was performed in the crystallizer illustrated in Fig. 2, part of the supersaturated region of the dissolved product component of $Ni_{1/3}Mn_{1/3}Co_{1/3}(OH)_2$ distributed in the crystallizer contacted the tank bottom wall of the tank. On its wall, a deposition reaction of $Ni_{1/3}Mn_{1/3}Co_{1/3}(OH)_2$ occurred, and brown precipitation traces were formed.

Fig. 5(b) shows the simulation results of the supersaturated region under the crystallizer layout and experimental conditions of Case A. A series of simulations show the results of a parameter study of the coefficient α_1 in Eq. (7). The CFD results show three isosurfaces for the reaction ratios of the precipitation reactions shown in Eq. (7): dark green, medium green, and light green indicate regions where the reaction ratio exceeds 30%, 70%, and 90%, respectively. In this study, the model coefficient α_1 was set to 0.1, so that the contact area with the tank wall for the region with a 90% reaction ratio (light green) was consistent with that of the observation results for the precipitation traces. Furthermore, the isosurface of the $Ni_{1/3}Mn_{1/3}Co_{1/3}(OH)_2$ dissolved product component was drawn by overlapping the region where the reaction ratio exceeded 90%, and its concentration was found to be order of 0.01 mol/m^3.

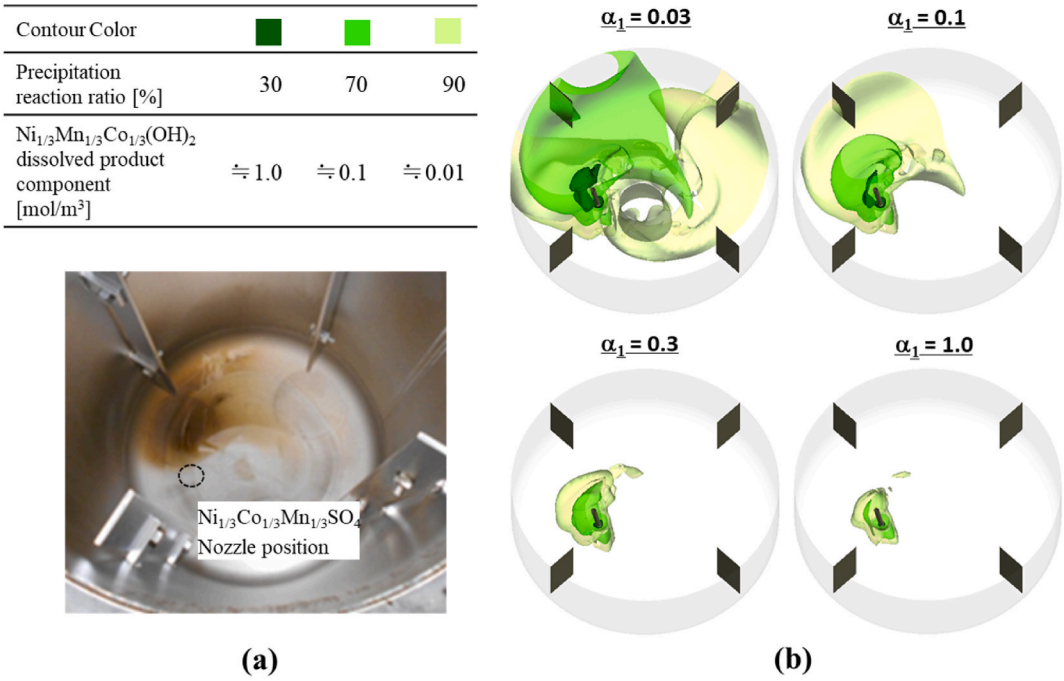

Fig. 5. Comparison of the distribution of the precipitation reaction ratio calculated by CFD and the shape of $Ni_{1/3}Mn_{1/3}Co_{1/3}(OH)_2$ precipitation traces on the walls observed in experiment. (a) Photograph of the $Ni_{1/3}Mn_{1/3}Co_{1/3}(OH)_2$ precipitation traces on the bottom of the crystallizer observed in the experiment in Case A; (b) The isosurface of the ratio of the precipitation reaction for CFD results varying α_1 in Case A.

5. Prediction of the particle size of $Ni_{1/3}Mn_{1/3}Co_{1/3}(OH)_2$ using the agglomeration model

5.1. Materials and methods

For secondary agglomeration, individual primary aggregates that comprise the secondary agglomerate must collide and coagulate. At the moment when primary aggregates collide with each other, the particle pairs are considered to be in weak connection owing to van der Waals forces. However, in the $Ni_{1/3}Mn_{1/3}Co_{1/3}(OH)_2$ precipitation, which is the subject of this study, the reaction operation is performed with strong agitation. Therefore, the particle pairs are immediately decoupled by the agitation action, because van der Waals force cannot solely maintain particle contacts. Moreover, in the reaction crystallization tank, a supersaturated region is formed by the dissolved product component of $Ni_{1/3}Mn_{1/3}Co_{1/3}(OH)_2$. If the primary aggregates collide with each other as they pass through this region, while the particles maintain connect owing to van der Waals forces, surface deposition occurring on the particle pairs causes bridging to be formed and strengthens the particles contact by chemical bonding forces. In the agglomeration model proposed by Mumtaz et al. [16] the driving force that produces the binding of particle pairs is considered to be the chemical bonding force owing to surface deposition, and the influence of van der Waals forces is no longer included in the model. In the agglomeration model proposed by David et al. [17], the contact mode of particle pairs, which affects the sticking probability, is based on bridging by surface deposition.

Some of the particle pairs that are strengthened by surface deposition endure decoupling by the hydrodynamic forces associated with agitation. However, as the size of secondary agglomerate increases, the hydrodynamic forces acting on the agglomerate become larger. Therefore, even if the bonding of particle pairs is strengthened by surface deposition, it will become insufficient to overcome the decoupling of particles owing to hydrodynamic action, and the size limit for growth as secondary agglomerate will be reached. David et al. [17] noted that in the reaction crystallization of adipic acid, the binding of agglomerates larger than the Kolmogorov scale is ruptured by hydrodynamic forces.

In this study, a particle growth model was developed assuming that the final size of secondary aggregates determined by the balance between the binding energy increased by surface deposition on the particle pairs and the breaking up energy that tends to decouple the particle pairs owing to hydrodynamic action induced by strong agitation.

5.1.1. Binding energy model

When the particles pass through the supersaturated region of $Ni_{1/3}Mn_{1/3}Co_{1/3}(OH)_2$, they collide with each other, and deposition occurs on the particle surface, causing them to agglomerate.

Fig. 6 illustrates this process. The $Ni_{1/3}Mn_{1/3}Co_{1/3}SO_4$ aqueous solution supplied from the feed nozzle reacts quickly with NaOH by neutralization, forming a highly supersaturated region of the $Ni_{1/3}Mn_{1/3}Co_{1/3}(OH)_2$ dissolved product component near the nozzle (darkest green region in Fig. 6). Downstream of this region, the degree of supersaturation gradually decreased because of precipitation reactions and turbulent dispersion. Because the bridging strength of particle pairs are affected by the time the agglomerate is exposed to the supersaturated region and the degree of supersaturation in that region, its history should be considered. Baldyga and Makowski [23] used CFD to calculate the distribution of supersaturated regions in a reaction crystallizer and analyzed their effect on grain size growth in a model case of the reaction crystallization of barium sulfate.

In this study, the binding energies of the particle pairs were estimated using the CFD results for the supersaturated region of the $Ni_{1/3}Mn_{1/3}Co_{1/3}(OH)_2$ dissolved product component. First, the region of the $Ni_{1/3}Mn_{1/3}Co_{1/3}(OH)_2$ dissolved product component calculated by CFD was divided into 18 regions for each level of the averaged concentration $\overline{C_{c,i}}$. The lower limit of the concentration level (i = 1) was set to approximately 0.01 mol/m^3, which corresponds to the concentration at the contour of the region with 90% reaction ratio of precipitation. The upper limit of the concentration level (i = 18) was set to 2.5 mol/m^3 so that the maximum concentration value in all the CFD results could be covered. Subsequently, V_i which is the volume of the averaged concentration of the dissolved

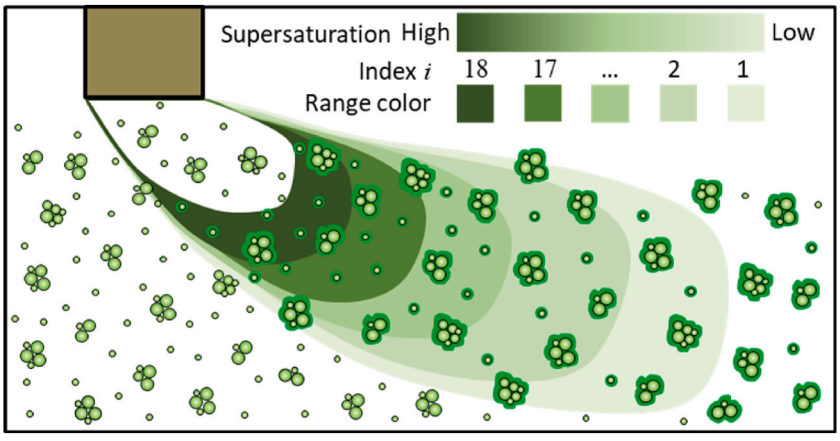

Fig. 6. Schematic of particle growth by secondary agglomeration in the supersaturated region.

product components $\overline{C_{c,i}}$ and the values related to the turbulent flow in each region were obtained from the CFD results. These values were applied to the model to determine the binding energies of the particle pairs as described below.

Fig. 7 illustrates particle bridging. Consider that a primary aggregate (radius r) contacts a secondary agglomerate (radius R) and binds chemically in the surface deposition layer of thickness h. When the particle bridging breaks up, the binding energy E_{bi} [J] is considered equal to the increase in surface energy.

$$E_{bi} = 2\Gamma S, \tag{8}$$

where Γ [J/m^2] is the surface energy per unit surface area of the particles, which is determined by the composition and crystal structure of the hydroxide. In this study, Γ is treated as a constant.

David et al. [17] assumed that particle bridging was cylindrical and proposed a function to describe the behavior of the change in the shape of particle bridging by the deposition reaction. Mumtaz et al. [16] approximated the contact point of particles as the contact between the vertices of a cone and proposed a 1-D model to describe the behavior of the change in distance to the contact point and the contact angle with the deposition reaction.

By contrast, the $Ni_{1/3}Mn_{1/3}Co_{1/3}(OH)_2$ primary aggregates and secondary agglomerates, which were the subject of this study, had a complex surface with a dense network of plate-like crystals. Therefore, it is impractical to represent the bridging growth function geometrically. This study proposes terms expressed in a simple form for the bridging growth function, as described below. The binding area S for particle bridging was assumed to be a circular cross section represented by the gray line in Fig. 7. S is expressed by the following equation based on the geometric relationship between the primary aggregate radii r, secondary agglomerate radii R and the thickness h of the surface deposition layer:

$$S = 4\pi \frac{rR}{r+R} h. \tag{9}$$

Considering that the secondary agglomerate is sufficiently large compared with the primary aggregate, r/R can be approximated as 0.

$$S = 4\pi r h. \tag{10}$$

The thickness h_i of the surface deposition layer in region i with $\overline{C_{c,i}}$ is proportional to the growth rate κ_i [m/s] of crystal deposition and the residence time t_i [s] of the agglomerate in region i.

$$h_i = \kappa_i t_i. \tag{11}$$

Because t_i is affected by the distribution of $\overline{C_{c,i}}$, the modeling of t_i focuses on the turbulent dispersion of the chemical components after being fed from the nozzle. Baldyga and Bourne [24,25] proposed a meso-mixing time scale τ_d related to turbulent mixing between the raw material solution fed through the nozzle and the surrounding bulk fluid under a uniform flow field and isotropic turbulence.

$$\tau_d = \frac{F}{u D_t}, \tag{12}$$

where F [m^3/s] is the volumetric flow rate of the liquid from the feed nozzle, D_t is the turbulent diffusion coefficient, and u is the bulk fluid velocity. This study assumes that the meso-mixing time τ_d is proportional to the summation of each residence time t_i in the part of the plume in region i, and t_i is expressed using V_i, $\overline{u_i}$ and $\overline{D_{t,i}}$.

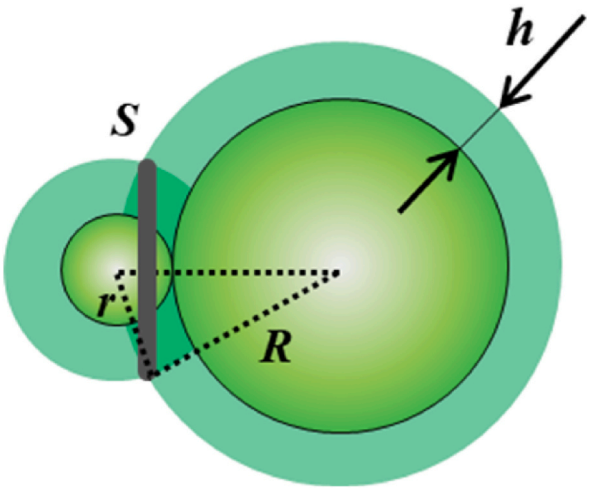

Fig. 7. Particle bridging.

$$\tau_d \propto \sum_{i=1}^{\infty} t_i \propto t_i = \frac{V_i}{\overline{u_i}\overline{D_{t,i}}}, \tag{13}$$

where $\overline{u_i}$ and $\overline{D_{t,i}}$ are the averaged values of the flow velocity and the turbulent diffusion coefficient in region i, respectively. If the raw material solution is fed from N_n nozzles, the volumetric flow rate per nozzle is F/N_n. Therefore, Eqs. (12) and (13) can be reorganized as Eq. (14):

$$t_i = \alpha_2 \sqrt{\frac{1}{N_n}\frac{V_i}{\overline{u_i}\overline{D_{t,i}}}}, \tag{14}$$

where α_2[-] is the proportional coefficient in this model.

The growth rate owing to surface deposition κ_i is expressed by the following equation based on the molecular diffusion of dissolved product components in the boundary layer formed on the agglomerate surface:

$$\kappa_i = \frac{1}{\rho_p} D_c \frac{\overline{C_{c,i}}}{R}. \tag{15}$$

By reorganizing Eqs. ((8), (10), (11), (14) and (15), Eq. (16) was obtained for the binding energy of the agglomerate:

$$E_{bi} = A\frac{r}{R}\sum_{i=1}^{\infty}\overline{C_{c,i}}\sqrt{\frac{1}{N_n}\frac{V_i}{\overline{u_i}\overline{D_{t,i}}}}, \tag{16}$$

where the model coefficient A ($=8\pi\alpha_2\Gamma D_c/\rho_p$) is used to summarize the physical properties and other constants.

5.1.2. Breaking up energy model

Primary aggregates or secondary agglomerate move along with the fluid flow formed in the reaction crystallizer. Shear or elongational flows act on agglomerate riding on the fluid flow, causing the restructuring and breakup of the agglomerate [26]. Horii et al. [27] simulated the restructuring of agglomerate by the surrounding flow and showed that the agglomerate was squashed after a complex restructuring process and elongated along the streamline. Mumtaz et al. [16] focused on tensile forces based on hydrodynamics and introduced a model for the probability of successful aggregation in the reaction crystallization of calcium oxalate. Based on hydrodynamics, this study also focuses on tensile forces affecting the agglomeration.

In a stirred-tank-type reaction crystallizer, the agglomerate circulating with fluid flow are accelerated along the streamline by the force received from the impeller as they pass through the impeller. This study assumed that part of this force acts to elongate secondary agglomerate and break up the bonds of the particle pairs; the breakup energy E_{br} is expressed as in the following equation:

$$E_{br} = \alpha_3 \rho_p \frac{4\pi}{3}\left(r^3 + R^3\right)\frac{d\overline{u}}{dt}L_p, \tag{17}$$

where α_3 [-] is the model coefficient that indicates the ratio of the force received by the agglomerate from the impeller which breaks up the particle pairs. It is estimated that α_3 varies depending on the impeller type and presence of baffles. In this study, α_3 was treated as a constant because only standard type of the Rushton turbine impeller was used, and the layout involving the impeller and baffles was not changed. du/dt [m/s^2] denotes the acceleration of the agglomerate. L_p [m] is the characteristic length at which the agglomerate is accelerated, and this study set the L_p to the radius of the impeller.

The acceleration that the agglomerate receive as they pass through the impeller is estimated to depend on the shape, scale, and rotational speed of the impeller. According to the dimensional analysis using L_p and rotation speed ω [s^{-1}], the acceleration of the agglomerate received in the flow direction can be modeled to be proportional to L_p and ω^2.

$$\frac{d\overline{u}}{dt} = \alpha_4 L_p \omega^2, \tag{18}$$

where α_4 denotes the proportionality coefficient. The impeller type did not change in this study, therefore, α_4 was treated as a constant. Considering that secondary agglomerate are sufficiently large compared with the primary aggregates, this study approximates $r^3+R^3 \approx R^3$. Finally, Eq. (19) for the breaking up energy model was obtained by reorganizing Eqs. (17) and (18):

$$E_{br} = BR^3\omega^2 L_p^2, \tag{19}$$

where B (= $4\pi\alpha_3\alpha_4\rho_p/3$) is the model coefficient expressed as a group of constants.

5.1.3. Balance of the binding energy and breaking up energy

Based on the concept that the size of secondary aggregate at the end of agglomeration stage ($t/t_{term} = 0.1$) is determined when the binding energy of bridging of the primary aggregates, which constitute the secondary agglomerate, is balanced by the energy to break them apart, Eq. (20) was obtained by $E_{bi} = E_{br}$ connecting Eqs. (16) and (19).

$$R = \left[Ar \sum_{i=1}^{\infty} \overline{C_{c,i}} \sqrt{\frac{1}{N_n} \frac{V_i}{\overline{u_i} \overline{D_{t,i}}}} \Big/ B\omega^2 L_p^2 \right]^{\frac{1}{4}}. \tag{20}$$

In other words, Eq. (20) assumes that the diameter of secondary aggregates ($2R$) at the end of the agglomeration stage ($t/t_{term} = 0.1$) is determined proportionally to E_{bi}/E_{br}. In the experimental precipitation of $Ni_{1/3}Mn_{1/3}Co_{1/3}(OH)_2$ described in Section 3, the size of the secondary aggregate at the end of the agglomeration stage obtained under the reference conditions was set to R_0. In this study, the ratio R/R_0 in Eq. (20) was used to obtain Eq. (21). In other words, the ratio of $2R$ under other conditions to $2R_0$ under reference conditions (R/R_0) is assumed to be proportional to the ratio of E_{bi}/E_{br} and E_{bi0}/E_{br0}. The model coefficients A and B and the size of the primary aggregates r were assumed to be constant, regardless of the precipitation conditions.

$$\frac{R}{R_0} = \frac{\left[\sum_{i=1}^{\infty} \overline{C_{c,i}} \sqrt{\frac{1}{N_n} \frac{V_i}{\overline{u_i} \overline{D_{t,i}}}} \Big/ \omega^2 L_p^2 \right]^{\frac{1}{4}}}{\left[\sum_{i=1}^{\infty} \overline{C_{c0,i}} \sqrt{\frac{1}{N_{0,n}} \frac{V_{0,i}}{\overline{u_{0,i}} \overline{D_{t0,i}}}} \Big/ \omega_0^2 L_{0,p}^2 \right]^{\frac{1}{4}}}. \tag{21}$$

In this study, the following variables were calculated using CFD and substituted into Eq. (21): They refer to the concentration of the $Ni_{1/3}Mn_{1/3}Co_{1/3}(OH)_2$ dissolved product component distributed in the crystallizer ($\overline{C_{c,i}}$, $\overline{C_{c0,i}}$), region volume of $\overline{C_{c,i}}$, $\overline{C_{c0,i}}$ (V_i, V_{0i}), average flow velocity ($\overline{u_i}, \overline{u_{0,i}}$), and turbulent diffusion coefficient ($\overline{D_{t,i}}$, $\overline{D_{t0,i}}$) in the region of $\overline{C_{c,i}}$, $\overline{C_{c0,i}}$. Thereafter, the size of the secondary aggregate at the end of the agglomeration stage (R) that precipitates under a specific condition can be determined as the ratio of increase or decrease from the aggregate at the end of the agglomeration stage (R_0) under the reference condition.

5.2. Results and discussion

5.2.1. Prediction of the size of secondary aggregates using the particle agglomeration model

Fig. 8 shows the parity plots of the experimental and calculated results for the ratio of the size of secondary aggregate at the end of the agglomeration stage ($t/t_{term} = 0.1$). The calculation results were obtained from Eq. (21). To determine the size ratio, R/R_0, the secondary aggregates precipitated in Case A were used as the reference size, R_0. The dotted line in Fig. 8 indicates the boundary at which the calculated value deviates from the experimental value by ± 20%. The calculated values from the model constructed in this study tend to be larger than the experimental values but can be predicted within a range of ±20% of the difference. This result confirms that the size of the secondary aggregate formed in the end of the agglomeration stage of the $Ni_{1/3}Mn_{1/3}Co_{1/3}(OH)_2$ precipitation by stirred-tank semi-batch reaction crystallization operation can be determined by a model constructed for the concept in which the binding energy of the particle pairs based on surface deposition in the supersaturated region is balanced by the breaking up energy acting when the agglomerate pass through an impeller. Furthermore, this model made it possible to quantitatively estimate the effects of the size of secondary aggregates on the scale of the reaction crystallizer, feed rate of the raw material liquids, number of feed nozzles, and agitation power.

Based on the method proposed in this study, once the size of secondary aggregate at the end of the agglomeration stage ($t/t_{term} = 0.1$) is determined, the number of secondary aggregates can be estimated by the value of the total amount of raw material solution

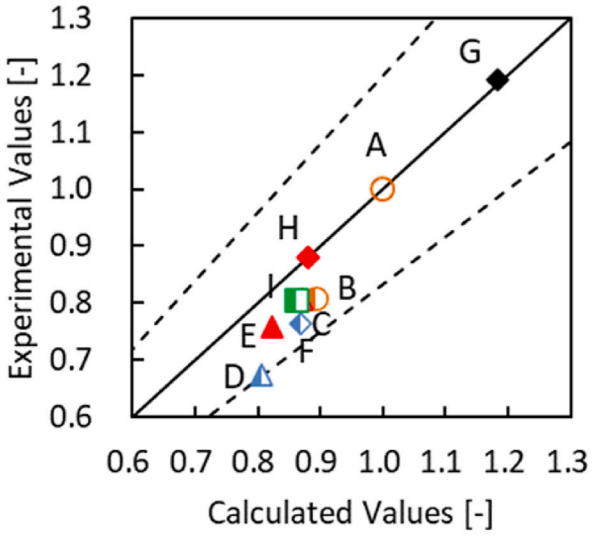

Fig. 8. Parity plots of the ratio of the size of secondary aggregate at the end of the agglomeration stage.

supplied to the reactor up to that point divided by the apparent density and volume of secondary aggregate. Then, the size and number of secondary aggregates can be estimated, the total surface area of the secondary aggregates can be determined, and the size of the rounded aggregation by surface deposition can be estimated.

5.2.2. *Distribution of the supersaturated region and its effect on agglomerate size*

5.2.2.1. Flow rate of raw material solution. The concentration distribution of the $Ni_{1/3}Mn_{1/3}Co_{1/3}(OH)_2$ dissolved product component was calculated using CFD in Cases D and F, where N_n and P_v were the same, and only V_T/F was different. The V_T/F ratio in Case D is 1.72 and that in Case F is 0.86. Fig. 9 shows the isosurfaces of the $Ni_{1/3}Mn_{1/3}Co_{1/3}(OH)_2$ dissolved product components at three molar concentrations (0.01, 0.1, and 1.0 mol/m^3). Fig. 9(a) and (b) show the calculation results for cases D and F, respectively. In both cases, a plume of the $Ni_{1/3}Mn_{1/3}Co_{1/3}(OH)_2$ dissolved product component formed from the tip of the feed nozzle to the area close to the impeller. The plume was distributed over a wider area in Case F, where the V_T/F ratio was lower. Fig. 9(c) shows the volume ratios of the plume of the $Ni_{1/3}Mn_{1/3}Co_{1/3}(OH)_2$ dissolved product components for Cases D and F classified by $\overline{C_{c,i}}$. The volume of the plume in Case F was larger than that in Case D at all concentrations. Particularly, the volume was more than twice as large at concentrations greater than 0.05 mol/m^3. Under the same stirring conditions, that is the same distribution of uD_t, a larger plume volume indicates a longer characteristic time t_i expressed in Eq. (14). This result suggests that the agglomerate is exposed to higher supersaturated regions for longer periods as they pass through the regions. The longer duration promotes bridging of the agglomerate and increases the secondary aggregate size at the end of the agglomeration stage ($t/t_{term} = 0.1$).

5.2.2.2. Agitation power. The concentration distribution of the $Ni_{1/3}Mn_{1/3}Co_{1/3}(OH)_2$ dissolved product component was calculated by CFD in Cases G and H, where V_T/F and N_n were the same, and only P_v was different. The P_v ratio in Case G was 0.40 and that in Case H was 1.26. Fig. 10(a) and (b) show the calculation results for cases G and H, respectively. As shown in Fig. 10(c), the volume ratio of the plume of the $Ni_{1/3}Mn_{1/3}Co_{1/3}(OH)_2$ dissolved product component was similar, despite the comparison under conditions of approximately three times P_v.

Fig. 11 shows the isosurfaces of uD_t, which is a variable of the turbulent flow field, at three levels of degree (0.10, 0.15, and 0.20 m^3/s^2). Fig. 11(a) and (b) show the calculation results for Cases G and H, respectively. In the stirred-tank of the same scale, the agitation power increased as the impeller speed increased. Thus, both the flow velocity u and turbulent diffusion coefficient D_t increased. Fig. 11(c) shows the ratio of $\overline{u_i}\overline{D_{t,i}}$ in the plume region of the $Ni_{1/3}Mn_{1/3}Co_{1/3}(OH)_2$ dissolved product component classified by $\overline{C_{c,i}}$ for Cases G and H. In Case G, under relatively strong agitation conditions, all levels of plumes were exposed to a high $\overline{u_i}\overline{D_{t,i}}$. A larger $\overline{u_i}\overline{D_{t,i}}$ with the same plume volume implies a shorter characteristic time t_i as expressed in Eq. (14). This shortened characteristic time leads to a decrease in the binding energy of particles. In addition, increasing the agitation power promotes the breakup of the bridging. Consequently, the bridging is suppressed, and the secondary aggregate size at the end of the agglomeration stage ($t/t_{term} = 0.1$) is smaller.

5.2.2.3. Number of nozzles. The concentration distribution of the $Ni_{1/3}Mn_{1/3}Co_{1/3}(OH)_2$ dissolved product component was calculated by CFD in Cases A and B, where V_T/F and P_v were the same, and only N_n was different. N_n in Case A was 1, and in Case B it was 4. Fig. 12 (a) shows the calculation results for Case A and Fig. 12(b) shows the calculation results for Case B. As shown in Fig. 12(c), the volume ratio of the plume of the $Ni_{1/3}Mn_{1/3}Co_{1/3}(OH)_2$ dissolved product component does not decrease when the feed solution is fed from multiple nozzles. Rather, the volume ratio of the plume increases at concentrations below 0.1 mol/m^3. However, the volume of the plume formed per nozzle decreases. This result indicates that even if V_i and $\overline{u_i}\overline{D_{t,i}}$ are the same as that in Eq. (14), the characteristic time t_i will decrease as N_n increases. This decrease in the characteristic time suppresses the bridging, resulting in smaller secondary

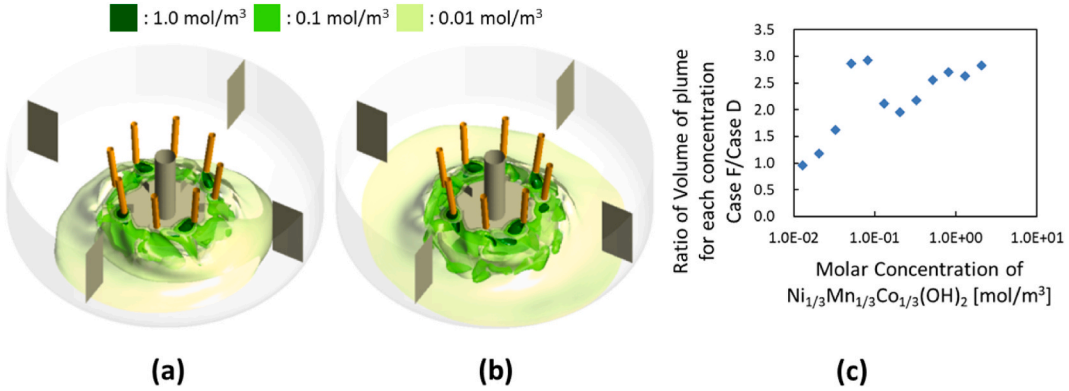

Fig. 9. Comparison of $Ni_{1/3}Mn_{1/3}Co_{1/3}(OH)_2$ dissolved product component plumes in Cases D and F. (a) Isosurfaces of molar concentration of $Ni_{1/3}Mn_{1/3}Co_{1/3}(OH)_2$ dissolved product component in Case D; (b) in Case F; (c) The volume ratios of the plume of the $Ni_{1/3}Mn_{1/3}Co_{1/3}(OH)_2$ dissolved product components for Cases D and F.

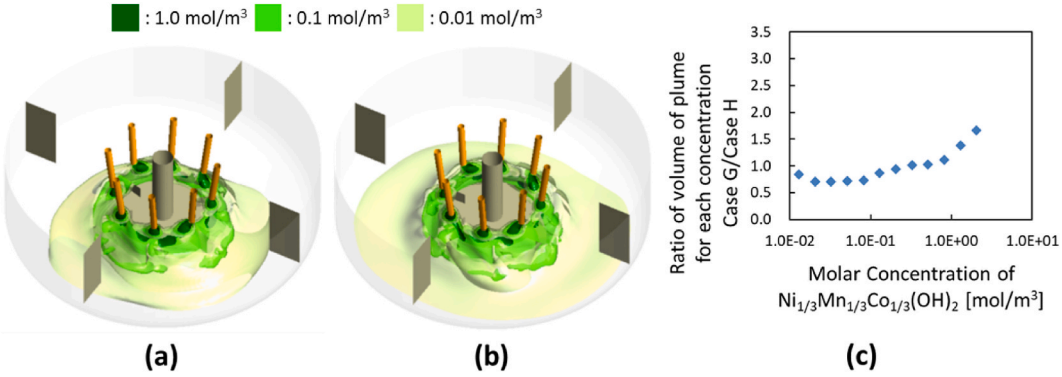

Fig. 10. Comparison of $Ni_{1/3}Mn_{1/3}Co_{1/3}(OH)_2$ dissolved product component plumes in Cases G and H. (a) Isosurfaces of molar concentration of $Ni_{1/3}Mn_{1/3}Co_{1/3}(OH)_2$ dissolved product component in Case G; (b) in Case H; (c) The volume ratios of the plume of the $Ni_{1/3}Mn_{1/3}Co_{1/3}(OH)_2$ dissolved product components for cases G and H.

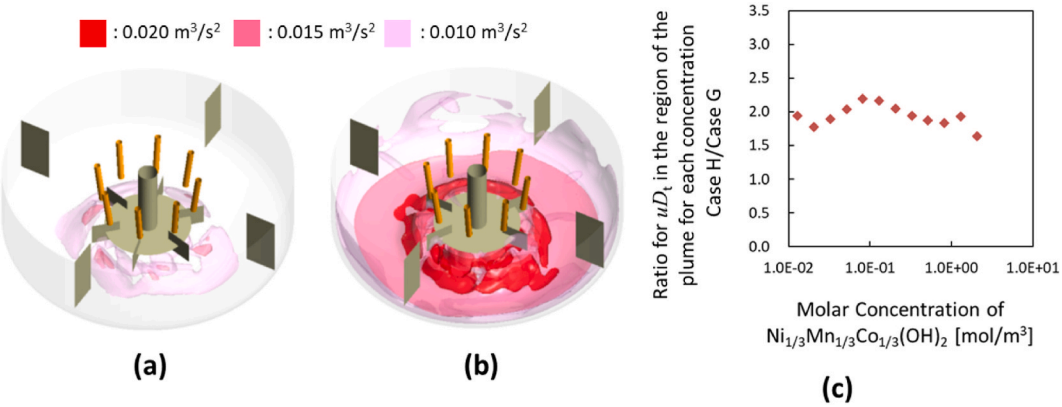

Fig. 11. Comparison of the distribution of uD_t in Cases G and H. (a) Isosurfaces of uD_t in Case G; (b) in Case H; (c) The ratios of $\overline{u_i}\overline{D_{t,i}}$ in the plume region of the $Ni_{1/3}Mn_{1/3}Co_{1/3}(OH)_2$ dissolved product components for cases G and H.

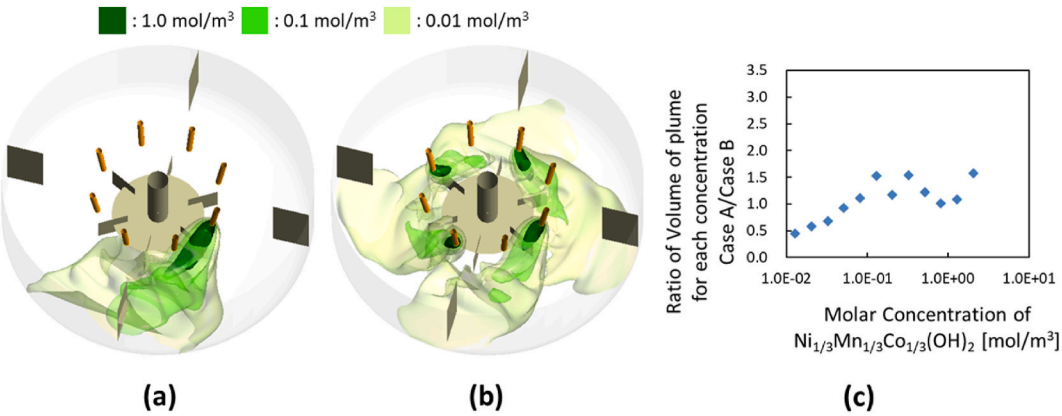

Fig. 12. Comparison of $Ni_{1/3}Mn_{1/3}Co_{1/3}(OH)_2$ dissolved product component plumes in Cases A and B. (a) Isosurfaces of molar concentration of $Ni_{1/3}Mn_{1/3}Co_{1/3}(OH)_2$ dissolved product component in Case A; (b) in Case B; (c) The volume ratios of the plume of the $Ni_{1/3}Mn_{1/3}Co_{1/3}(OH)_2$ dissolved product components for cases A and B.

aggregate size at the end of the agglomeration stage ($t/t_{term} = 0.1$).

6. Conclusions

In this study, the $Ni_{1/3}Mn_{1/3}Co_{1/3}(OH)_2$ reaction crystallization process in a stirred-tank semi-batch reaction crystallizer is divided into a nucleation stage (t/t_{term}: 0.0–0.02), an agglomeration stage (t/t_{term}: 0.02–0.1), and a surface deposition stage (t/t_{term}: 0.1–1.0), and a method was developed to predict the size of secondary aggregates at the end of the agglomeration stage ($t/t_{term} = 0.1$), which dominate the final size of the $Ni_{1/3}Mn_{1/3}Co_{1/3}(OH)_2$ particles. The method consists of a three-step procedure described below.

In the first step, a CFD model was constructed, consisting of the governing equations of hydrodynamics and the mass balance of the chemical components. In the mass balance of the chemical components, production by the neutralization reaction and consumption by the precipitation reaction were considered for the $Ni_{1/3}Mn_{1/3}Co_{1/3}(OH)_2$ dissolved product component, which is a supersaturated component. The distribution of supersaturated regions formed in the reaction tank reaches a steady state sufficiently fast compared to the rise in liquid level associated with semi-batch reaction crystallization. Therefore, a geometry model fixed at the liquid volume (1/3 of the tank capacity) at the end of the agglomeration stage ($t/t_{term} = 0.1$) was used to quantify the pseudo-steady state dissolved product component distribution and turbulent flow field formed in the crystallizer.

In the second step, a particle growth model that focus on the secondary agglomeration in the reaction crystallization of $Ni_{1/3}Mn_{1/3}Co_{1/3}(OH)_2$ was developed. The model is based on the concept that the size of the secondary aggregate at the end of the agglomeration stage ($t/t_{term} = 0.1$) is determined by the balance between the binding energy of the particle pairs, which is strengthened by surface deposition on the pair as the agglomerate pass through the supersaturated region, and the breaking up energy of the particle pairs owing to the hydrodynamic force brought about by agitation. Based on this hypothesis, the balance of the number of primary aggregates and the amount of precipitation affects the secondary agglomeration rate but not the final size of secondary agglomerates. In addition, when the size and apparent density of the primary aggregates are constant, it is not necessary to consider the balance of the number of primary aggregates and the amount of precipitation to determine the final size of secondary agglomerates.

In the final step for validation, the information on the turbulent flow field and the concentration distribution of the $Ni_{1/3}Mn_{1/3}Co_{1/3}(OH)_2$ dissolved product component formed in the crystallizer identified by CFD were assigned to the agglomeration model to predict the size of the secondary aggregate at the end of the agglomeration stage ($t/t_{term} = 0.1$). This study succeeded in predicting the experimental results on the size of the $Ni_{1/3}Mn_{1/3}Co_{1/3}(OH)_2$ secondary aggregate within ±20% difference; the secondary aggregate was precipitated via stirred-tank-type semi-batch reaction crystallization under the following experimental parameters: scale of the crystallizer, feeding conditions of the raw material solution, and stirring conditions.

The following issues must be addressed to further enhance the applicability of this model: herein, the model coefficient α_1 of the precipitation reaction rate was adjusted such that the shape of the supersaturated region calculated by CFD corresponds to the precipitation traces on the wall of the crystallizer observed in the experiment. However, this method requires an experiment to deposit the precipitation traces on the wall of the crystallizer, which is laborious to set up. Furthermore, depending on the type of reaction system, depositing the precipitation traces on the wall may not be possible. Conversely, if the actual neutralization and precipitation reaction rates for each operating conditions can be measured, the model coefficient α_1 can be determined without using precipitation traces, which is expected to improve the applicability of the model.

Further, the analysis in this study was based on the premise that the reaction crystallizer is scaled up through geometric similarity. However, to predict particle size, including cases where the shape of the impeller and the placement of nozzles relative to the impeller vary, the model coefficients α_2, α_3, and α_4 of the particle agglomeration should not be considered constant, but their dependency on the layout of the crystallizer should be investigated.

In future work, we plan to develop a method for quantitatively measuring the actual neutralization and precipitation reaction rates. In addition, we plan to investigate the effect of altering the impeller type and the arrangement of the feed nozzles of the crystallizer on the particle size. Through these efforts, we expect to further enhance the applicability of the particle size prediction method proposed herein.

The analysis of semi-batch reaction crystallization systems of $Ni_xMn_yCo_z(OH)_2$ of any composition, not limited to $Ni_{1/3}Mn_{1/3}Co_{1/3}(OH)_2$ should be possible by adjusting the model parameters according to the procedure developed in this study.

Data availability statement

The datasets supporting this study are presented in the article.

Funding

This research did not receive any specific funding.

CRediT authorship contribution statement

Kazuhiko Tsuchioka: Writing – original draft, Validation, Software, Methodology, Investigation, Conceptualization. **Kazuhide Hayashi:** Supervision, Project administration. **Ryuta Misumi:** Writing – review & editing, Supervision, Data curation.

Declaration of competing interest

The authors declare the following financial interests/personal relationships which may be considered as potential competing interests: Kazuhiko Tsuchioka has patent #JPA 2020037496 issued to Sumitomo Metal Mining Co. Ltd.

Acknowledgements

We are grateful to M. Yoshida, T. Ono and S. Ozawa for technical assistance with the experiments. We also thank K. Maki for mentoring support in conducting this study.

References

[1] M. Hietaniemi, T. Hu, J. Välikangas, J. Niittykoski, U. Lassi, Effect of precursor particle size and morphology on lithiation of $Ni_{0.6}Mn_{0.2}Co_{0.2}(OH)_2$, J. Appl. Electrochem. 51 (2021) 1545–1557, https://doi.org/10.1007/s10800-021-01596-4.
[2] Y. Koshika, H. Kaneda, S. Yoshio, Y. Furuichi, Precursor morphology control and electrochemical properties of $LiNi_{0.35}Mn_{0.30}Co_{0.35}O_2$ as a Li-ion battery positive electrode material, ACS Appl. Energy Mater. 5 (2022) 8169–8177, https://doi.org/10.1021/acsaem.2c00698.
[3] M. Nie, Y. Xia, Z. Wang, F. Yu, Y. Zhang, J. Wu, B. Wu, Effects of precursor particle size on the performance of $LiNi_{0.5}Co_{0.2}Mn_{0.3}O_2$ cathode material, Ceram. Int. 41 (2015) 15185–15192, https://doi.org/10.1016/j.ceramint.2015.08.093.
[4] N. Yabuuchi, Y. Koyama, N. Nakayama, T. Ohzuku, Solid-state chemistry and electrochemistry of $LiCo_{1/3}Ni_{1/3}Mn_{1/3}O_2$ for advanced lithium-ion batteries II. Preparation and characterization, J. Electrochem. Soc. 152 (2005) A1434–A1440, https://doi.org/10.1149/1.1924227.
[5] G. Yang, X. Qin, B. Wang, F. Cai, J. Gao, Well-ordered spherical $LiNi_{0.8}Co_{0.1}Mn_{0.1}O_2$ cathode material for lithium-ion batteries, J. Mater. Res. 35 (2019) 51–57, https://doi.org/10.1557/jmr.2019.307.
[6] M.-H. Lee, Y.-J. Kang, S.-T. Myung, Y.-K. Sun, Synthetic optimization of $Li[Ni_{1/3}Co_{1/3}Mn_{1/3}]O_2$ via co-precipitation, Electrochim. Acta 50 (2004) 939–948, https://doi.org/10.1016/j.electacta.2004.07.038.
[7] L. Liang, K. Du, Z. Peng, Y. Cao, J. Duan, J. Jiang, G. Hu, Co–precipitation synthesis of $Ni_{0.6}Co_{0.2}Mn_{0.2}(OH)_2$ precursor and characterization of $LiNi_{0.6}Co_{0.2}Mn_{0.2}O_2$ cathode material for secondary lithium batteries, Electrochim. Acta 130 (2014) 82–89, https://doi.org/10.1016/j.electacta.2014.02.100.
[8] J.H. Mugumya, M.L. Rasche, R.F. Rafferty, A. Patel, S. Mallick, M. Mou, J.A. Bobb, R.B. Gupta, M. Jiang, Synthesis and theoretical modelling of suitable co-precipitation conditions for producing NMC111 cathode material for lithium-ion batteries, Energy Fuels 36 (2022) 12261–12270, https://doi.org/10.1021/acs.energyfuels.2c01805.
[9] Y. Yang, S. Xu, M. Xie, Y. He, G. Huang, Y. Yang, Growth mechanisms for spherical mixed hydroxide agglomerates prepared by co-precipitation method: a case of $Ni_{1/3}Co_{1/3}Mn_{1/3}(OH)_2$, J. Alloys Compd. 619 (2015) 846–853, https://doi.org/10.1016/j.jallcom.2014.08.152.
[10] P. Barai, Z. Feng, H. Kondo, V. Srinivasan, Multiscale computational model for particle size evolution during coprecipitation of li-ion battery cathode precursors, J. Phys. Chem. B 123 (2019) 3291–3303, https://doi.org/10.1021/acs.jpcb.8b12004.
[11] K. Tsuchioka, K. Maki, S. Nakakura, Prediction of particle size distribution by use of a model of precipitation by collision and coagulation, Kagaku Kogaku Ronbunshu 44 (2018) 45–49, https://doi.org/10.1252/kakoronbunshu.44.45.
[12] M. Shiea, A. Querio, A. Buffo, G. Boccardo, D. Marchisio, CFD-PBE modelling of continuous Ni-Mn-Co hydroxide co-precipitation for Li-ion batteries, Chem. Eng. Res. Des. 177 (2022) 461–472, https://doi.org/10.1016/j.cherd.2021.11.008.
[13] R. Zauner, A.G. Jones, Scale-up of continuous and semibatch precipitation processes, Ind. Eng. Chem. Res. 39 (2000) 2392–2403, https://doi.org/10.1021/ie990431u.
[14] R. Zauner, A.G. Jones, Mixing effects on product particle characteristics from semi-batch crystal precipitation, Chem. Eng. Res. Des. 78 (2000) 894–902, https://doi.org/10.1205/026387600527969.
[15] Z. Wu, Y. Zhou, J. Zeng, C. Hai, Y. Sun, X. Ren, Y. Shen, X. Li, Investigating the effect of pH on the growth of coprecipitated $Ni_{0.8}Co_{0.1}Mn_{0.1}(OH)_2$ agglomerates as precursors of cathode materials for Li-ion batteries, Ceram. Int. 49 (2023) 15851–15864, https://doi.org/10.1016/j.ceramint.2023.01.180.
[16] H.S. Mumtaz, M.J. Hounslow, N.A. Seaton, W.R. Paterson, Orthokinetic aggregation during precipitation, 2, Chem. Eng. Res. Des. 75 (1997) 152–159, https://doi.org/10.1205/026387697523615.
[17] R. David, P. Marchal, J.P. Klein, J. Villermaux, Crystallization and precipitation engineering—III. A discrete formulation of the agglomeration rate of crystals in a crystallization process, Chem. Eng. Sci. 46 (1991) 205–213, https://doi.org/10.1016/0009-2509(91)80130-Q.
[18] F.R. Menter, Two-equation eddy-viscosity turbulence models for engineering applications, AIAA J. 32 (1994) 1598–1605, https://doi.org/10.2514/3.12149.
[19] B.F. Magnussen, B.H. Hjertager, On mathematical modeling of turbulent combustion with special emphasis on soot formation and combustion, Symposium (International) on Combustion 16 (1977) 719–729, https://doi.org/10.1016/S0082-0784(77)80366-4.
[20] D.B. Spalding, Mixing and chemical reaction in steady confined turbulent flames, Symposium (International) on Combustion 13 (1971) 649–657, https://doi.org/10.1016/S0082-0784(71)80067-X.
[21] W.E. Ranz, W.R. Marshall Jr., Evaporation from drops, Chem. Eng. Prog. 48 (1952) 141–146.
[22] J.D. Bernal, J. Mason, Packing of spheres: Co-ordination of randomly packed spheres, Nature 188 (1960) 910–911, https://doi.org/10.1038/188910a0.
[23] J. Bałdyga, Ł. Makowski, W. Orciuch, Interaction between mixing, chemical reactions, and precipitation, Ind. Eng. Chem. Res. 44 (2005) 5342–5352, https://doi.org/10.1021/ie049165x.
[24] J. Bałdyga, J.R. Bourne, Interactions between mixing on various scales in stirred tank reactors, Chem. Eng. Sci. 47 (1992) 1839–1848, https://doi.org/10.1016/0009-2509(92)80302-S.
[25] J. Bałdyga, J.R. Bourne, Turbulent Mixing and Chemical Reaction, Wiley, Chichester, 1999.
[26] K. Higashitani, K. Iimura, H. Sanda, Simulation of deformation and breakup of large aggregates in flows of viscous fluids, 56, Chem. Eng. Sci. 56 (2001) 2927–2938, https://doi.org/10.1016/S0009-2509(00)00477-2.
[27] K. Horii, R. Yamada, S. Harada, Strength deterioration of nonfractal particle aggregates in simple shear flow, Langmuir 31 (2015) 7909–7918, https://doi.org/10.1021/acs.langmuir.5b00197.